12th International Symposium on Turbulence and Shear Flow Phenomena (TSFP12)
Osaka, Japan, July 19–22, 2022

LAGRANGIAN STATISTICS OF SUPERSTRUCTURES IN A TURBULENT BOUNDARY LAYER WITH PRESSURE GRADIENTS

Matthew Bross[1], Matteo Novara[2], Daniel Schanz[2], Felix Eich[1], Andreas Schröder[2] & Christian J. Kähler[1]

[1]Institute of Fluid Mechanics and Aerodynamics
Universität der Bundeswehr München
85577 Neubiberg, Germany
[2]Institute of Aerodynamics and Flow Technology
German Aerospace Center (DLR)
37073 Göttigen, Germany
matthew.bross@unibw.de, matteo.novara@dlr.de, daniel.schanz@dlr.de, felix.eich@googlemail.com,
andreas.schroeder@dlr.de & christian.kaehler@unibw.de

Abstract

In the log-law region of turbulent boundary layers, streamwise elongated flow regions of high- and low-momentum can extent up to several boundary layer thicknesses. They are often referred to as superstructures. These structures contain a relatively large portion of the layer's turbulent kinetic energy and have been shown to interact with the near-wall features. In the last few decades these structures have been extensively analyzed for the zero-pressure gradient turbulent boundary layer condition. However by comparison, the structural characteristics for adverse pressure gradient turbulent boundary layer flows are much less studied. Therefore, the three-dimensional dynamics of turbulent superstructures in a turbulent boundary layer flow are investigated in the Atmospheric Wind Tunnel Munich (AWM) using a novel multi-camera 3D time-resolved Lagrangian particle tracking approach. In this study, Lagrangian statistics will be used to characterize the dynamics and interaction of turbulent superstructures within a zero pressure gradient (ZPG) turbulent boundary layer at $\mathrm{Re}_\tau = 5460$ or $\mathrm{Re}_\theta = 13\,300$ that then flows over a curved plate subjected to a favorable (FPG) and strong adverse (APG) pressure gradient, which eventually separates. The main research aim is to determine if mass and momentum transfer between the superstructures exists. It was found that the dispersion of single particles along trajectories in the log-law layer are capable of moving more than the average Eulerian superstructure spacing in the spanwise direction. Furthermore, single particle dispersion structure functions indicate that, on average, the maximum dispersion in the spanwise direction is due to trajectories originating in the log-law layer. This implies that the highly energetic turbulent superstructures are responsible for a significant amount of the dispersion or mixing present in the turbulent boundary layer.

Introduction

Large-scale coherent structures present in zero pressure gradient (ZPG) turbulent boundary layers have been studied extensively in the past decades and many statistical and structural properties of the flow are well known (Wallace, 2012; Adrian *et al.*, 2000; Ganapathisubramani *et al.*, 2005; Hutchins & Marusic, 2007*a*). A remarkable property of the superstructures is their streamwise length, which is on average about $6\delta - 8\delta$. However, instantaneously they can extend up to $10\delta - 20\delta$ in the streamwise direction. In addition, they strongly meander in the spanwise direction (Eich *et al.*, 2020; Kevin *et al.*, 2019) and it has been shown that they can carry a relatively large a portion of the layer's turbulent kinetic energy, especially at large Reynolds numbers (Hutchins *et al.*, 2011). In effect, these large-scale structures are the main contribution to the formation of the second plateau/peak in the streamwise velocity fluctuations in the log-law layer, which appears at high Reynolds numbers (Fernholz & Finley, 1996; Samie *et al.*, 2018). Furthermore, an interaction between superstructures and the near-wall dynamics has been demonstrated (Hutchins & Marusic, 2007*b*; Bross *et al.*, 2019). Therefore, the investigation of these superstructures is important for understanding the overall dynamics of turbulent boundary layers. Moreover, it has been shown that turbulent superstructures can modulate the instantaneous turbulent flow separation line (Eich & Kähler, 2020).

In comparison to the large amount of investigations about the coherence of superstructures in the Eulerian reference frame, a Lagrangian description of these structures is largely absent from the literature. Which is largely due to the technical challenges involved in large-scale Lagrangian measurements of high-Reynolds number turbulent flows. However, analysis of Lagrangian flow statistics and related coherent structures are important for understanding mixing and mass transport in turbulent systems (Biferale *et al.*, 2008; Haller, 2015). This understanding is particularly relevant for engineering applications related to pollutant dispersion, the formation of large-scale meteorological systems, and both industrial and natural mixing processes (Yeung, 2002; Toschi & Bodenschatz, 2009). Therefore, using an experiment involving 12 cameras and 3 overlapping sub-volumes (Schanz *et al.*, 2019) and the evaluation of the data using novel Lagrangian particle tracking methods (Schanz *et al.*, 2016), a unique data set has been created for the investigation of both Eulerian and Lagrangian descriptions of coherent flow structures. In the following sections, statistics of Lagrangian trajectories within in a turbulent boundary layer subjected to ZPG, FPG, and APG will be analyzed and connected to the presence of elongated superstructures within the flow.

Experimental Setup

The experiments were conducted in the Atmospheric Wind Tunnel Munich (AWM), which is an Eiffel type wind tunnel located at the Universität der Bundeswehr München. The test section is 22 m long and the cross-section area measures 1.85 m $\times$ 1.85 m. To achieve a pressure gradient distribution, a turbulent boundary layer model, consisting of two S-shaped flow deflections, was installed in the wind tunnel side wall. The model was designed by Knopp *et al.* (2018) by means of RANS simulations. In between the flow deflections, a 4 m long flat plate is installed over which zero pressure gradient conditions are present, see figure 1. The flow velocity in this investigation was set to 14 m/s in the bulk flow over the ZPG section, resulting in a Reynolds number, $\mathrm{Re}_\tau = 5460$ or

Re_θ = 13 300 in the ZPG region. Upstream historical effects have been shown to influence the shape/topology of the wake region of this boundary layer but for this Reynolds number it was shown that the turbulent behavior in the near-wall and log-law layer remains largely unaffected (Knopp *et al.*, 2022)

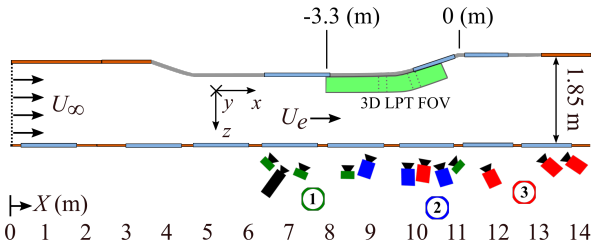

Figure 1: 3D-time-resolved Lagrangian particle tracking experimental setup. Measurements were preformed in the Atmospheric Wind Tunnel Munich (AWM).

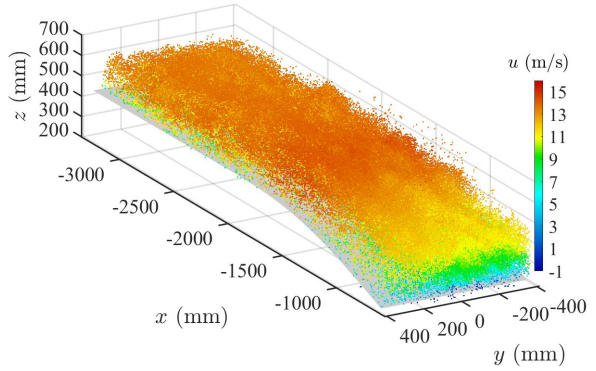

Figure 2: Instantaneous particle trajectory field colored with streamwise velocity u.

The flow was measured using a novel multi-camera multi-volume 3D Lagrangian particle tracking (LPT) technique that was able to capture a flow volume 2.9 m by 0.8 m by 0.25 m in the streamwise (x), spanwise (y) and wall-normal (z) directions respectively. An imaging system consisting of 12 high-speed cameras was used to record particle images from helium filled soap bubbles (HFSB) tracers illuminated by 10 high-powered LED arrays. This allows for the observation of turbulent superstructures in the ZPG region as they travel through the FPG and APG regions. A sketch of the camera arrangement and field-of-view is shown in figure 1. An exemplary instantaneous plot of the particle trajectories colored with streamwise velocity u is shown in figure 2 which shows the deceleration of the tracer particles in the diffuser region. The Reynolds stress profiles are provided in figure 3 to illustrate that the near-wall (down to $z^+ \approx 15$) flow properties can be resolved with the LPT measurement employed here. A table of calculated and estimated near and far field flow parameters are given in table 1. The values presented represent an average over the ZPG region.

For each run, approximately 2700 time steps were recorded at 2000 Hz. The large effort of planning and performing the measurements were a part of a joint campaign between the UniBw and the DLR. The 3D reconstruction of individual particle tracers from the images recorded by the multi-camera system has been carried out by the DLR using an in-house implementation of the Shake-the-Box (STB) algorithm (Schanz *et al.*, 2016). The post-processing of the trajectory data and further evaluation presented herein was performed by UniBw. More details about the experimental setup, calibration, and Lagrangian particle tracking can be found in Schanz *et al.* (2019).

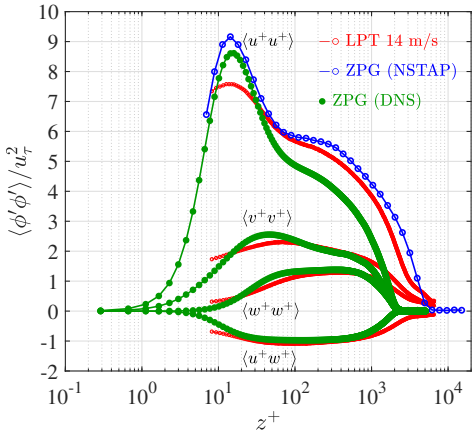

Figure 3: Reynolds stresses in viscous scaling for the ZPG region. The present experiment (LPT 14 m/s) is at Re_τ = 5460. In addition, hotwire (NSTAP) measurements at Re_τ = 6000 (Samie *et al.*, 2018) and DNS computations at $\mathrm{Re}_\tau \approx 2000$ (Sillero *et al.*, 2013) of a ZPG turbulent boundary layer are plotted.

Table 1: Flow field properties averaged over ZPG region.

BL thickness	δ_{99}	[m]	0.171
edge velocity	U_e	[m/s]	13.9
unit Reynolds num.	Re_{x_e}	[−]	1.51×10^5
mom. Reynolds num.	Re_θ	[−]	13 300
friction Reynolds num.	Re_τ	[−]	5460
viscous unit	ν/u_τ	[μm]	31.3
friction velocity	u_τ	[m/s]	0.5
rec. frequency	f	[Hz]	2000
time lag	τ	[ms]	0.5
viscous time lag	τ^+	[−]	8
Kolmogorov time scale	τ_η	[ms]	0.032
BL eddy turnover time	T_L	[ms]	12.3

Single Particle Lagrangian Dispersion

The dispersion of single particles along trajectories in and around superstructures in a subsection of the entire flow volume is analyzed in this section. An approximately 1 meter section in the ZPG region was selected to study the trajectories passing through this volume over 150 times steps, corresponding to $\tau U_e/\delta_{99_{(ZPG)}} = 6$. The dispersion of a single particle from an initial streamwise release position $\mathbf{x_0}$ and time t_0 is defined as $\Delta X_i = X_i(\mathbf{x_0},\tau) - X_i(\mathbf{x_0},t_0)$. An exemplary plot of the dispersion value of subset of trajectories as a function of convective time is shown in figure 4.

In figure 5, trajectories in the log-law layer that travel through this region over 150 times steps, are plotted and colored with the streamwise fluctuation velocity u'. When a particle traveling along a trajectory exceeds a spanwise dispersion (ΔY) value of more that $0.25\delta_{99_{(ZPG)}}$, they are color coded in pink. Since the average Eulerian spanwise spacing of these superstructures is around $0.25\delta_{99_{(ZPG)}}$ (Bross *et al.*, 2021; Novara *et al.*, 2021) and the fact that some of the trajectories dis-

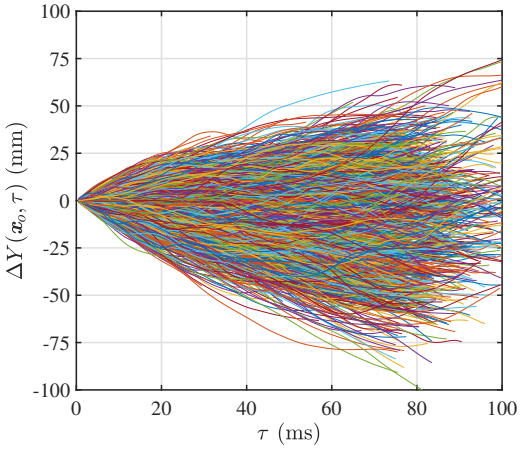

Figure 4: Single particle dispersion in the spanwise direction (ΔY) of all trajectories from a subset of a time series.

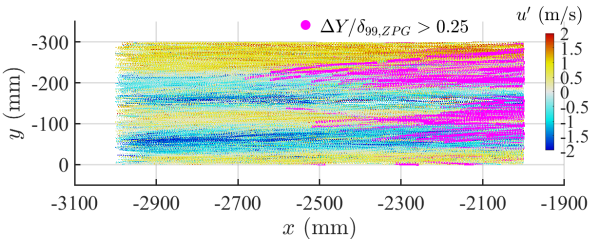

Figure 5: Trajectories in the log-law layer that travel through a 1 meter section of the ZPG region over 150 time steps ($\tau U_\infty/\delta_{99_{(ZPG)}} = 6$) colored with u'. Particles that exceed a spanwise dispersion, ΔY, value of more than $0.25\delta_{99_{(ZPG)}}$ are color coded in pink.

perse from their original position more than this value, i.e. the pink color coded locations in figure 5, it can be interpreted that there are mass and momentum exchanges between the superstructures but for the most part single particles remain confined within the superstructures.

To quantify the single particle dispersion in the wall normal (z) and spanwise (y) directions an ensemble (over all data sets) joint-histogram of dispersion in both directions as a function of convective time is shown in figures 6a − 6f. For consistency, the maximum count is used to normalize all the other bin values so that the color contour, P goes from 0 to 1. In addition, the development of the dispersion distribution in the ZPG region (-3000 m $\leq x \leq -2000$ m) is shown in figures 6a − 6c, and the subsequent FPG to APG (-2000 m $\leq x \leq -1000$ m) is shown in figures 6d − 6f.

As the dispersion distribution grows over time it is evident that many trajectories remain close to their initial position at τ = 0. In figure 6a the area inside white contour line (corresponding to P = 0.75), is located between $|\Delta Y|/\delta_{99_{(ZPG)}} < 0.1$ and $|\Delta Z|/\delta_{99_{(ZPG)}} < 0.05$. Therefore, it can be stated that the most probable spanwise and wall-normal dispersion values, over the shown time series, are not larger than the average spanwise superstructure spacing of $\Delta Y/\delta_{99_{(ZPG)}} = 0.25$ (Bross *et al.*, 2019). It could be then interpreted that most trajectories remain relatively close (i.e. low dispersion values) to their initial position due to their location within streamwise extended superstructures. Trajectories with larger dispersion values would then represent trajectories that move in between superstructures.

For the FPG/APG region shown in figures 6d − 6f the dispersion distribution in the spanwise direction looks very

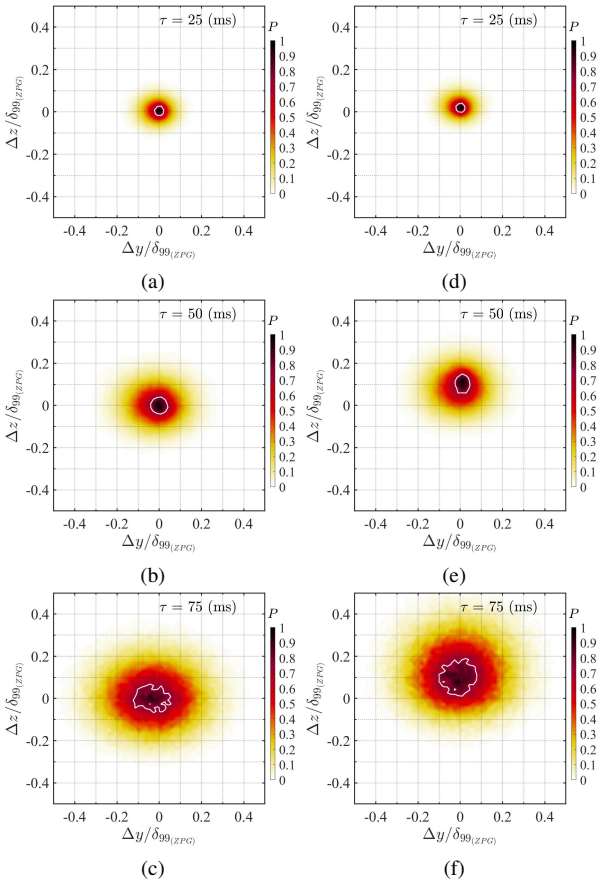

Figure 6: Joint-histogram of single particle dispersion in spanwise (y) and wall-normal (z) directions as a function of convective time for the (a − c) ZPG region (-3000 m $\leq x \leq -2000$ m) and (d − f) and the subsequent FPG to APG region (-2000 m $\leq x \leq -1000$ m). The maximum count is used to normalize all the other bin values so that the color contour, P goes from 0 to 1. Also shown in each plot is a white contour line corresponding to P = 0.75.

similar to the plots shown for the ZPG region in figures 6a − 6c. This indicates, that in terms of single particle dispersion, the trajectories are not modified in the spanwise direction due to pressure gradients when compared to the ZPG case. This is understandable when the history effects of the proceeding ZPG region are considered (Bobke *et al.*, 2017) and due to the fact that the superstructures retain their structural features, e.g. relative spacing, when subjected to strong pressure gradients (Eich & Kähler, 2020). However, in the wall-normal direction, the dispersion distribution is skewed towards positive ΔZ values for the FPG/APG region. This is likely due to the decelerating flow and thickening of the boundary layer in the APG region as the separation region is approached.

In figures 6a − 6f, all trajectories are used to calculated the dispersion distribution, but as the turbulence intensity depends on the wall normal location in a boundary layer (see figure 3) the following section will consider dispersion statistics as a function of initial wall normal location.

Structure Function

In order to analyze the statistical behavior of single particle dispersion, the second order structure given by $\langle \Delta X_i(z_0,\tau)^2 \rangle = \langle (X_i(z_0,\tau) - X_i(z_0,t_0))^2 \rangle$, as a function of the initial wall normal release location z_0 was computed from an

ensemble of all data sets over 150 time steps for ΔY and ΔZ. Since the turbulent fluctuation intensity depends on the wall normal position, see figure 3, the second order structure functions were computed as a function of the initial wall normal release position, z_0, in 10 mm bins ($0.06/\delta_{99_{(ZPG)}}$) and plotted in figures 7a and 7b. In these plots the reference location $\tau U_\infty/\delta_{99_{(ZPG)}} = 0$ corresponds to $x = -2000$ m, i.e. negative τ corresponds to the dispersion in the ZPG regions and positive τ corresponds to the FPG and APG region.

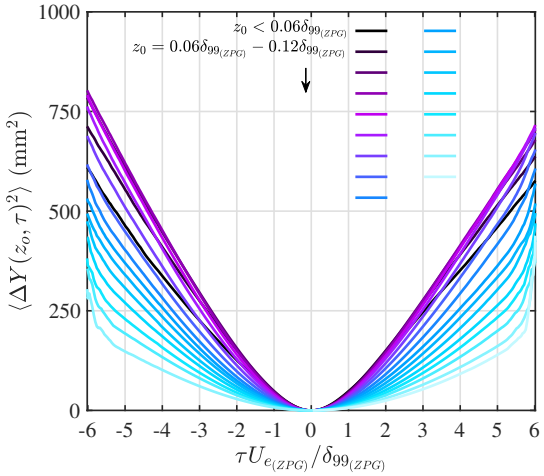

(a)

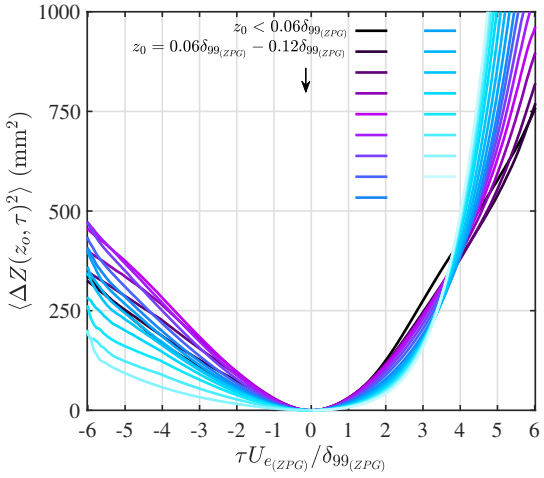

(b)

Figure 7: Second order structure function of single particle dispersion in the (a) spanwise and (b) wall normal directions vs. $\tau U_\infty/\delta_{99_{(ZPG)}}$ for different initial release locations in the wall normal direction z. Wall normal bins (z_0) have width of 10 mm or $0.06/\delta_{99_{(ZPG)}}$. Reference location $\tau U_\infty/\delta_{99_{(ZPG)}} = 0$ corresponds to $x = -2000$ m so negative τ corresponds to the dispersion in the ZPG regions and positive τ corresponds to the FPG and APG region.

In figure 7a values of the second order structure function, $\langle \Delta Y \rangle^2$, at z_0 bins near the wall increase until $z_0 = 0.18\delta_{99_{(ZPG)}} - 0.23\delta_{99_{(ZPG)}}$ and then gradually decrease as z_0 bin values approach the wake. This is also true for $\langle \Delta Y \rangle^2$ in the FPG/APG region shown in figure 7a. Since these bin are located in the log-law region, where the highly energetic superstructures are centered in, the maximum $\langle \Delta Y \rangle^2$ values coming from trajectories released in the log-law layer is understandable. The spanwise meandering of the superstructures is likely responsible for the elevated $\langle \Delta Y \rangle^2$ values. Furthermore, the spanwise structure function, $\langle \Delta Y \rangle^2$, looks almost symmetric about $\tau = 0$. In other words, its appears that spanwise dispersion is not modified from the ZPG to the FPG/APG regions. This is likely due to the fact that the Eulerian spanwise superstructure topological properties are also preserved in the strong APG flow following the ZPG region (Eich & Kähler, 2020; Bross *et al.*, 2021).

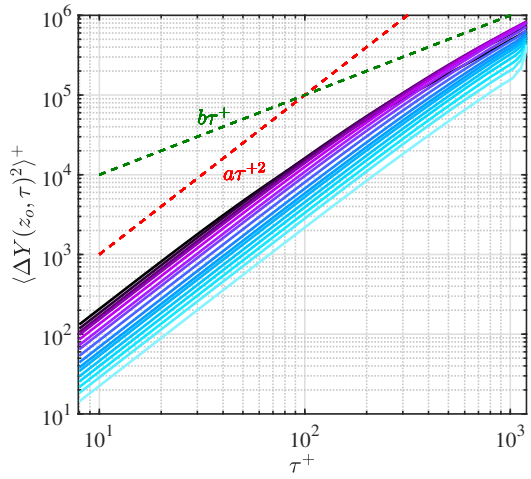

(a)

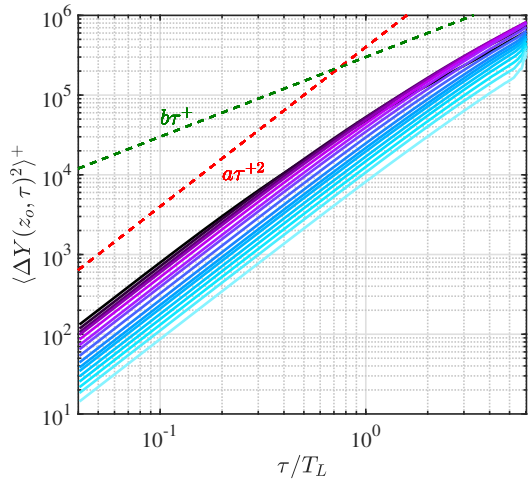

(b)

Figure 8: Second order structure function of single particle dispersion in the spanwise direction for different initial release locations in the wall normal direction z for the ZPG region with (a) inner/viscous and (b) boundary layer turnover time, T_L, time lag scaling.

As previously indicated by the joint-histogram analysis if figure 6f, the wall-normal structure function ($\langle \Delta Z \rangle^2$) is starkly different in the FPG/APG ($\tau > 0$) than the ZPG region. Interestingly, at around $\tau U_e/\delta_{99_{(ZPG)}} = 4$, bins near the wake region overtake the $\langle \Delta Z \rangle^2$ value of bins closer to the wall. Which means that, on average, trajectories originating in the wake region initially have less wall normal dispersion than trajectories closer to the wall, but after several eddy turn over times, those trajectories disperse more significantly in the wall normal direction than ones closer to the wall.

In figures 8a and 8b, $\langle \Delta Y \rangle^2$ in the ZPG region is plotted

in inner/viscous scaling while the time lags are scaled with inner/viscous and boundary layer or eddy turnover time T_L. In both plots, the axis are shown with a log-log scaling in order to better see short time lags ($\tau < T_L$). For short time lags ($\tau < T_L$) the second order structure function appears to vary quadratically with time and for larger time lags ($\tau > T_L$) the relationship appears linear. This is consistent with the predictions of Taylor (Taylor, 1922) for homogeneous isotropic turbulence (HIT).

Conclusions and Outlook

In this work, the 3D-dimensional flow structure of an evolving turbulent boundary layer from ZPG to FPG to APG and eventually flow separation, was studied using a novel large-FOV Lagrangian particle tracking technique. The large-volume allowed for the simultaneous tracking of large-scale turbulent superstructures in the streamwise, spanwise, and wall-normal directions. In addition to the average structure properties, this data set can be used to investigated the temporal evolution of superstructures. Furthermore, the availability of Lagrangian trajectories allows for the investigation of how individual trajectories behave and their relationship with the turbulent superstructures.

It was found that the dispersion of single particles along trajectories in the log-law layer are capable of motions that extend past the average Eulerian superstructure spacing in the spanwise direction. Which suggests that there is mass and momentum exchange between the high and low momentum superstructures. Moreover, it was found that the most probable dispersion values after roughly 6 boundary layer turnover times lie within an area corresponding to the average Eulerian superstructure width. The same conclusion can be made for the spanwise dispersion values in the FPG/APG region, suggesting that the superstructure topology is not modified from ZPG to APG for this model geometry.

Looking at the mean square or second order structure function of single particle dispersion, it is clear that maximum spanwise dispersion values occur within the log-law layer for both ZPG and FPG/APG regions. Furthermore, the scaling predicted by Taylor for HIT also appears to remain valid for the present case despite the highly aniostropic nature of a turbulent boundary layer.

In the future, analysis of the local trajectory path is needed in order to better identify full or parts of trajectories that lie inside or between coherent structures. Analysis of integral path lines, individual trajectory correlations, and dual particle dispersion might provide further information for the detection of Lagrangian coherent structures based on the characteristics of individual and groups of particle trajectories within the flow.

Acknowledgments

This work is supported by the Priority Programme SPP 1881 Turbulent Superstructures funded by the Deutsche Forschungsgemeinschaft project numbers KA1808/21 and SCHR1165/5. In addition, this work was partially funded by the DFG project number KA1808/14.

REFERENCES

Adrian, R. J., Meinhart, C. D. & Tomkins, C. D. 2000 Vortex organization in the outer region of the turbulent boundary layer. *J. Fluid Mech* **422**, 1–54.

Biferale, L., Bodenschatz, E., Cencini, M., Lanotte, A. S., Ouellette, N. T., Toschi, F. & Xu, H. 2008 Lagrangian structure functions in turbulence: A quantitative comparison between experiment and direct numerical simulation. *Phys. of Fluids* **20** (6), 065103.

Bobke, A., Vinuesa, R., Örlü, R. & Schlatter, P. 2017 History effects and near equilibrium in adverse-pressure-gradient turbulent boundary layers. *J. Fluid Mech.* **820**, 667–692.

Bross, M., Eich, F., Schanz, D., Novara, M., Schröder, A. & Kähler, C. J. 2021 Superstructures in turbulent boundary layers with pressure gradients. *PAMM* **20** (1), e202000257.

Bross, M., Fuchs, T. & Kähler, C. J. 2019 Interaction of coherent flow structures in adverse pressure gradient turbulent boundary layers. *J. Fluid Mech.* **873**, 287–321.

Eich, F. & Kähler, C. J. 2020 Large-scale coherent motions in turbulent boundary layers under an adverse pressure gradient up to flow separation. *Int. J. of Heat and Fluid Flow* **85**, 108645.

Eich, F., de Silva, C. M., Marusic, I. & Kähler, C. J. 2020 Towards an improved spatial representation of a boundary layer from the attached eddy model. *Phys. Rev. Fluids* **5**, 034601.

Fernholz, H. H. & Finley, P. J. 1996 The incompressible zero-pressure-gradient turbulent boundary layer: An assessment of the data. *Prog. in Aerospace Sciences* **32** (4), 245–311.

Ganapathisubramani, B., Hutchins, N., Hambleton, W. T., Longmire, E. K. & Marusic, I. 2005 Investigation of large-scale coherence in a turbulent boundary layer using two-point correlations. *J. Fluid Mech.* **524**, 57–80.

Haller, G. 2015 Lagrangian Coherent Structures. *Annual Review of Fluid Mech.* **47** (1), 137–162.

Hutchins, N. & Marusic, I. 2007*a* Evidence of very long meandering features in the logarithmic region of turbulent boundary layers. *J. Fluid Mech.* **579**, 1–29.

Hutchins, N. & Marusic, I. 2007*b* Large-scale influences in near-wall turbulence. *Phil. Trans. R. Soc. A* **365**, 647–664.

Hutchins, N., Monty, J. P., Ganapathisubramani, B., NG, H. C. H. & Marusic, I. 2011 Three-dimensional conditional structure of a high-Reynolds-number turbulent boundary layer. *J. Fluid Mech.* **673**, 255–285.

Kevin, K., Monty, J. & Hutchins, N. 2019 The meandering behaviour of large-scale structures in turbulent boundary layers. *J. Fluid Mech.* **865**, R1.

Knopp, T., Novara, M., Schanz, D., Schülein, E., Schröder, A., Reuther, N. & Kähler, C. J. 2018 *A New Experiment of a Turbulent Boundary Layer Flow at Adverse Pressure Gradient for Validation and Improvement of RANS Turbulence Models*, pp. 85–94. Springer, Cham.

Knopp, T., Schanz, D., Novara, M., Lühder, W., Strampe, L., Schülein, E., Schröder, A., Bross, M., Parikh, A., McLellan, D., Eich, F. & Kähler, C. J. 2022 Experimental and numerical investigation of turbulent boundary layers with strong pressure gradients. In *AIAA SCITECH 2022 Forum*.

Novara, M., Schanz, D., Geisler, R., Agocs, J., Eich, F., Bross, M., Kähler, C. J. & Schröder, A. 2021 Investigation of turbulent boundary layer flows with adverse pressure gradient by means of 3D Lagrangian particle tracking with Shake-The-Box. In *14th Inter. Symp. on PIV, August 1-5*.

Samie, M., Marusic, I., Hutchins, N., Fu, M. K., Fan, Y., Hultmark, M. & Smits, A. J. 2018 Fully resolved measurements of turbulent boundary layer flows up to $Re_\tau = 20000$. *J. Fluid Mech.* **851**, 391–415.

Schanz, D., Gesemann, S. & Schröder, A. 2016 Shake-The-Box: Lagrangian particle tracking at high particle image densities. *Exp. Fluids* **57**, 70.

Schanz, D., Novara, M., Geisler, R., Agocs, J., Eich, F., Bross, M., Kähler, C. J. & Schröder, A. 2019 Large-scale volumetric characterization of a turbulent boundary layer flow. In

13th Inter. Symp. on PIV, July 22-24, Munich, Germany.

Sillero, J. A., Jiménez, J. & Moser, R. D. 2013 One-point statistics for turbulent wall-bounded flows at Reynolds numbers up to $\delta^+ \approx 2000$. *Phys. of Fluids* **25** (10), 105102.

Taylor, G. I. 1922 Diffusion by continuous movements. In *Proc. of the London Math. Soc., vol. 2, no. 1, pp. 196–212*.

Toschi, F. & Bodenschatz, E. 2009 Lagrangian Properties of Particles in Turbulence. *Annual Review of Fluid Mech.* **41** (1), 375–404.

Wallace, J. M. 2012 Highlights from 50 years of turbulent boundary layer research. *J. Turbulence* **13**, 1–70.

Yeung, P. K. 2002 Lagrangian Investigations of Turbulence. *Annual Review of Fluid Mech.* **34** (1), 115–142.